Supporting Information

Facile Electrochemical Approach Based on Hydrogen-Bonded MOFs-Derived Tungsten Ethoxide/Polypyrrole-Reduced GO Nanocrystal for ppb Level Ammonium Ions Detection

Sara Maira Mohd Hizam [1,2] and Mohamed Shuaib Mohamed Saheed [1,3,*]

[1] Centre of Innovative Nanostructures and Nanodevices (COINN), Universiti Teknologi PETRONAS, Seri Iskandar 32610, Perak, Malaysia
[2] Department of Fundamental and Applied Sciences, Universiti Teknologi PETRONAS, Seri Iskandar 32610, Perak, Malaysia
[3] Department of Mechanical Engineering, Universiti Teknologi PETRONAS, Seri Iskandar 32610, Perak, Malaysia
* Correspondence: shuaib.saheed@utp.edu.my

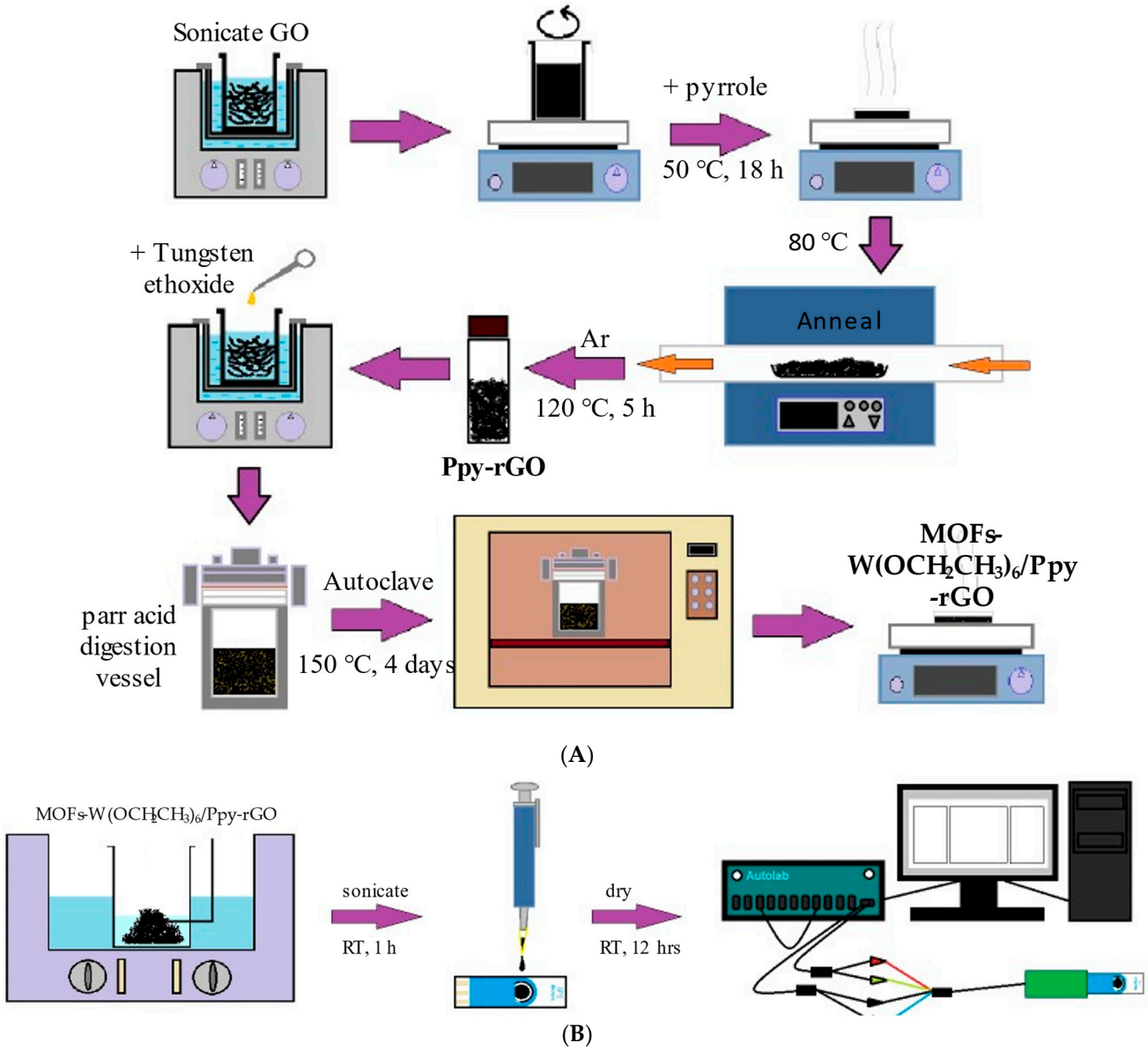

Figure S1. Schematic illustration of (**A**) preparation of MOFs−W(OCH$_2$CH$_3$)$_6$/Ppy−rGO−based electrochemical sensor device and analysis method, and (**B**) the schematic illustration of SPE device preparation and detection of NH_4^+ ions.

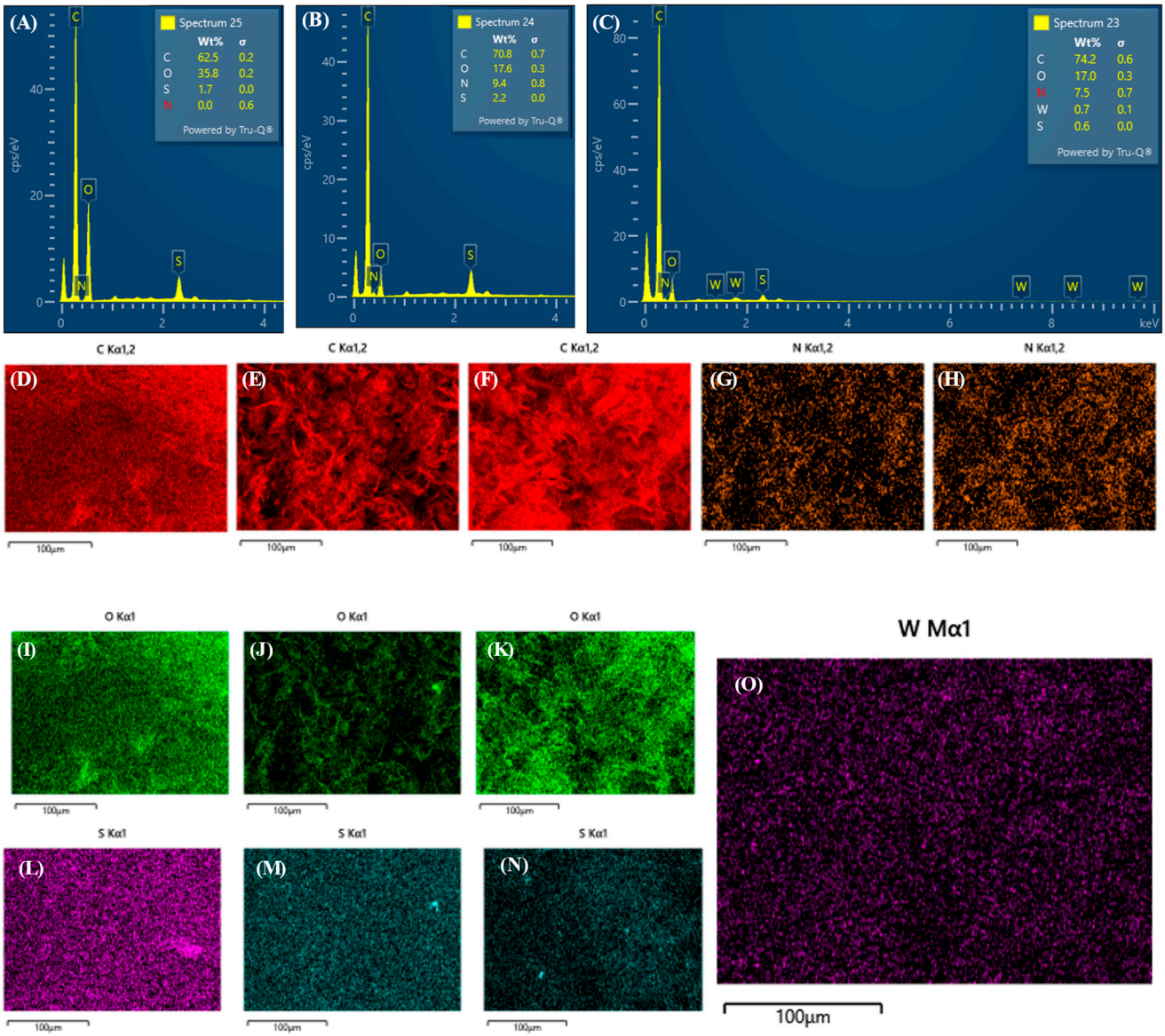

Figure S2. Compilation of EDX image of (**A**) GO, (**B**) Ppy−rGO, and (**C**) MOFs−W(OCH_2CH_3)$_6$/Ppy−rGO, and elemental mapping of carbon for (**D**) GO, (**E**) Ppy−rGO, and (**F**) MOFs−W(OCH_2CH_3)$_6$/Ppy−rGO; nitrogen for (**G**) Ppy−rGO, and (**H**) MOFs−W(OCH_2CH_3)$_6$/Ppy−rGO; oxygen for (**I**) GO, (**J**) Ppy−rGO, and (**K**) MOFs−W(OCH_2CH_3)$_6$/Ppy−rGO; sulfur for (**L**) GO, (**M**) Ppy−rGO, and (**N**) MOFs−W(OCH_2CH_3)$_6$/Ppy−rGO; and tungsten for (**O**) MOFs−W(OCH_2CH_3)$_6$/Ppy−rGO, respectively.

The well-prepared Ppy-rGO of 30 wt% is added to a well-dissolved tungsten ethoxide in N,N-dimethylformamide (DMF). Three weight percentage ratios have been analyzed, 30 wt%, 60 wt%, and 90 wt%. The D-band intensity in 30 wt% of the Raman spectrum is weaker than the intensity of the G-band. If the D-band intensity is weak and poorly sensitive to the excitation wavelength, this is most probably due to the high bonding ratio of heteroatoms such as nitrogen and oxygen. The spectrum pattern can be observed in the Raman spectra of GO and Ppy-rGO. As proven in other characterizations such as FTIR and XPS, the graphene lattice is highly bonded to oxygenated functional groups. For instance, the said oxygenated-functional groups are hydroxyl, carboxyl, and epoxy groups. The poorly sensitive excitation energy D-band reveals a lack of large graphitic domains. The highly sensitive G-band to excitation energy is due to the large amount of hydrogen bonding to the graphene lattice. However, the Raman spectra for 60 wt% and 90 wt% Ppy-

rGO addition show opposite results (Figure S2). There are more graphitic domains with the increased weight percentage of Ppy-rGO.

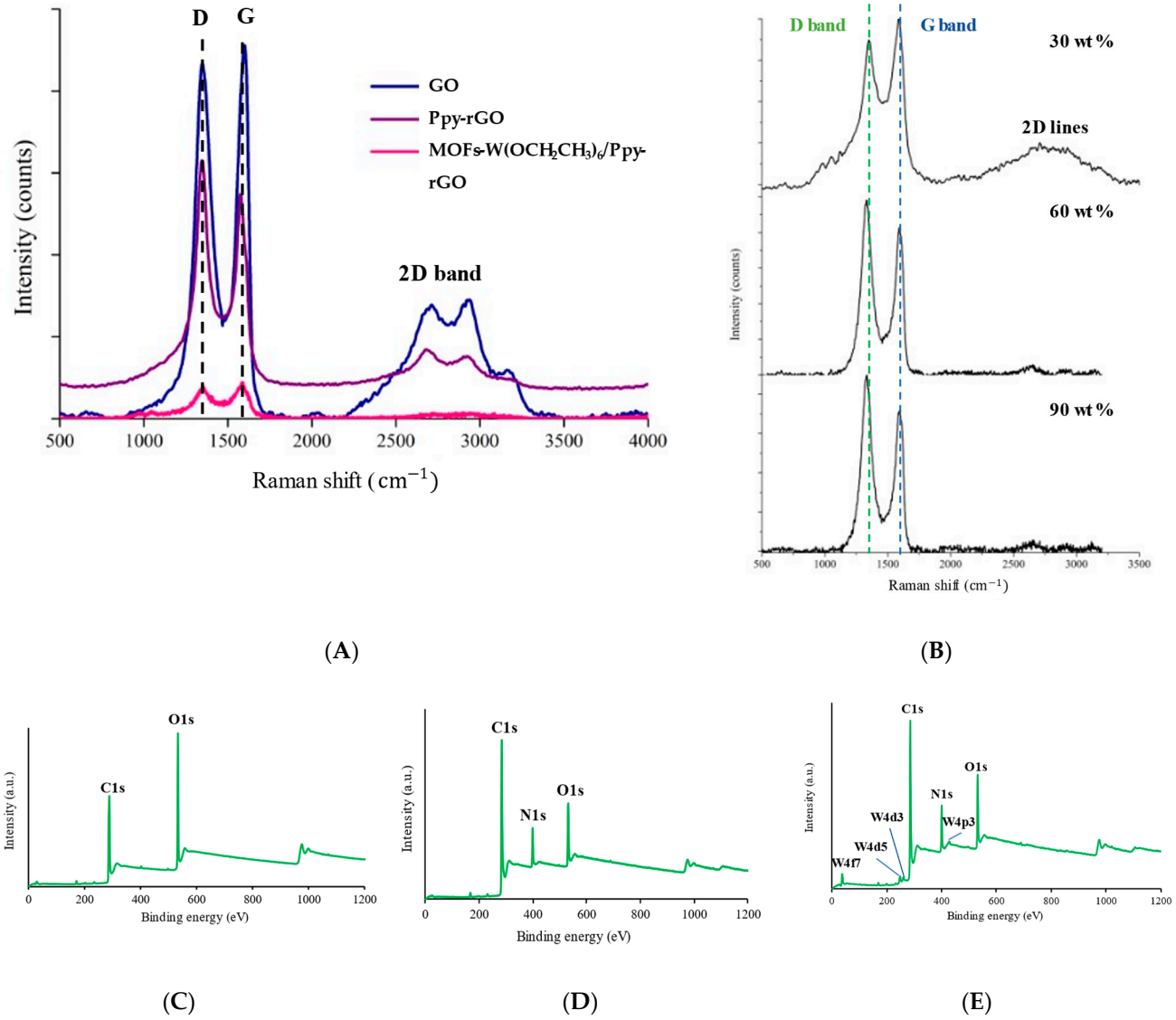

Figure S3. Full Raman spectra of (**A**) GO, Ppy-rGO, and MOFs-W(OCH_2CH_3)$_6$/Ppy-rGO, and (**B**) MOFs-W(OCH_2CH_3)$_6$/Ppy-rGO at 30 wt%, 60 wt%, and 90 wt% of Ppy-rGO added to tungsten ethoxide, and the full electron spectroscope for chemical analysis (SPCA) energy spectrum for (**C**) GO, (**D**) Ppy-rGO, and (**E**) MOFs-W(OCH_2CH_3)$_6$/Ppy-rGO.

A monolayer of graphene has two carbon atoms per unit cell, which consists of six phonon dispersion bands. Three of them are acoustic branches, and another three bands are optic phonon branches. The 2D line is the overtone of the D-band. It happens due to a double resonance or intervalley process that connects two points belonging to the same cone around the K point. In this double resonance process, the wave–vectors q of the phonons that are aligned with the D and 2D bands would couple preferentially to the electronic state with wave-vectors k measured at K point ($q \cong 2k$). The 2D Raman shape implies the existence of 2–5 graphene layers grown by the freeze-drying method [1]. The 2D bands, however, diminished as more reduction was applied. When the graphene layer stacking proliferates, the smaller peaks at lower frequencies decrease. Normally, for single-layer graphene, the 2D peak forms a single Lorentzian 2D peak. The peaks will be broader as the layers of graphene increase.

Table S1. Raman shifts and intensity ratios of GO, Ppy-rGO, and MOFs-W(OCH_2CH_3)$_6$/Ppy-rGO.

Nanocomposites	(cm^{-1})		I_D/I_G ratio
	D band	G band	
30 wt%	1352.5	1581.2	0.887
60 wt%	1328.6	1592.1	1.172
90 wt%	1336.2	1598.4	1.275

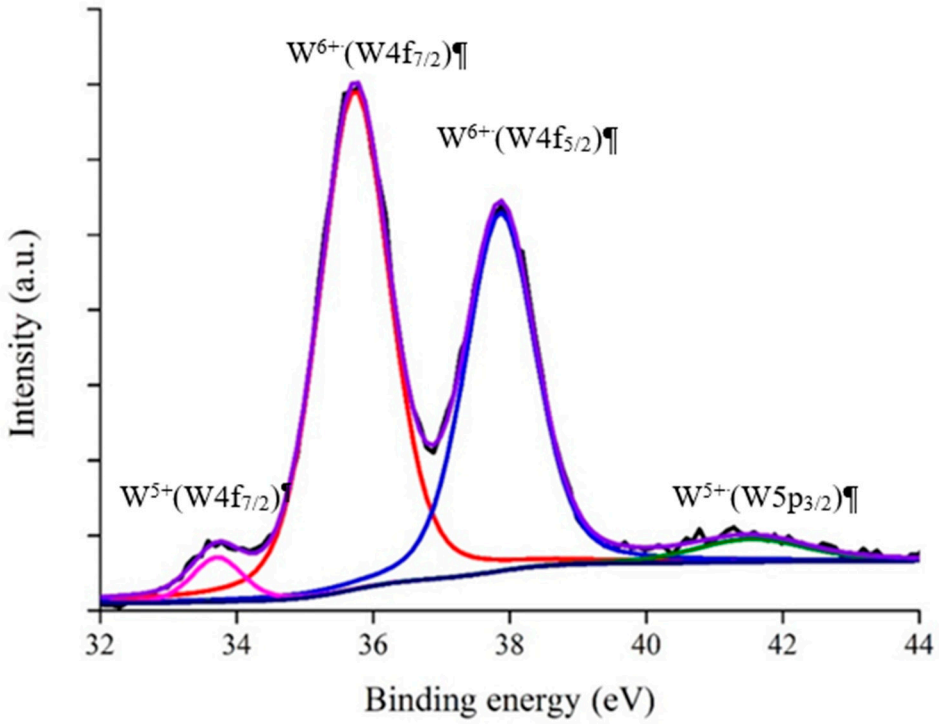

Figure S4. Deconvoluted narrow scan XPS spectrum of the W4f of MOFs-W(OCH_2CH_3)$_6$/Ppy-rGO.

X-ray diffraction (XRD) of the powder samples was recorded for 2θ values of 11.06° and 42.27° to characterize interplanar spacing. The characterization was executed in a PANalytical powder X-ray diffractometer at 45 keV and 20 mA with a step size of 0.01° and a dwell time of 5 s. Figure S5 shows the XRD patterns of GO, Ppy-rGO, and MOFs-W(OCH_2CH_3)$_6$/Ppy-rGO nanocomposites. Both Ppy-rGO and a strong peak at 2θ = 11.06° in XRD pattern of GO represent the (001) reflection of GO [2]. This peak vanishes upon the reduction of GO into rGO. Further, it can be found that there are two diffraction peaks, one being a broad diffraction peak located at 2θ = 26.03° and another being a small peak located at 2θ = 42.60°, present in both the Ppy-GO and MOFs-W(OCH_2CH_3)$_6$/Ppy-rGO spectra, which represent (002) and (100) reflection, respectively, which suggests the loss of hydroxyl and carboxyl groups in graphene nanostructures [3,4]. A small peak close to (002) reflection, which is located at 2θ = 18.53°, indicated the triclinic tungsten ethoxide combined with the diffraction peaks of rGO [5]. The triclinic phase of metal oxide is known to possess incredible stability and actively participate in sensing activity.

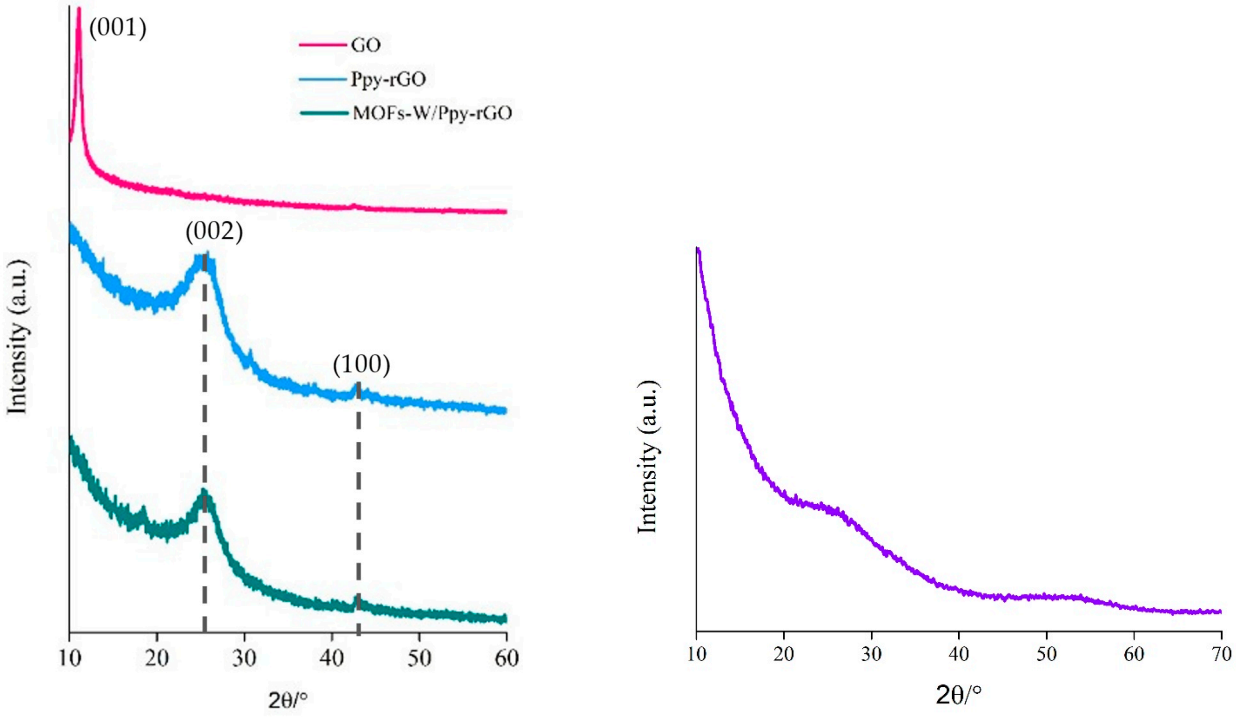

(**a**) (**b**)

Figure S5. XRD spectra of (**a**) GO, Ppy-rGO, and MOFs-W(OCH_2CH_3)$_6$/Ppy-rGO, and (**b**) W(OCH_2CH_3)$_6$.

Table S2. Crystallite size and XRD data of the triclinic phase of the nanocomposites.

Nanocomposites	Phase orientation			
	Bragg's angle (2θ)	FWHM (β)	d-spacing (Å)	Crsytallite size (Å)
GO	11.091	0.6373	7.971	135
	42.493	0.5766	2.126	162
Ppy-rGO	25.711	3.572	3.462	23
	42.719	0.533	2.115	124
MOFs-W(OCH_2CH_3)$_6$/Ppy-rGO	24.669	3.965	3.606	21
	42.693	1.802	2.116	49

Table S3. Empirical formula calculation based on CHNS/O database for GO, Ppy-rGO, and MOFs-W(OCH_2CH_3)$_6$/Ppy-rGO.

Sample	**GO**				
Element	**C**	**H**	**N**	**S**	**O**
Percentage (%)	42.79	2.107	0.007	1.862	38.099
Number of moles (mol)	$\frac{42.79}{12.01} = 3.563$	$\frac{2.107}{1.008} = 2.09$	$\frac{0.007}{14.01} = 0.0004 \approx 0$	$\frac{1.862}{32.06} = 0.058$	$\frac{38.099}{16.00} = 2.399$
Smallest ratio	$\frac{3.563}{0.058} = 61.431$	$\frac{2.09}{0.058} = 36.034$	0	$\frac{0.058}{0.058} = 1$	$\frac{2.399}{0.058} = 41.362$
Simplest ratio	61	36	0	1	41
Sample	Ppy-rGO				
Percentage (%)	54.164	1.434	2.895	1.975	26.954

Number of moles (mol)	$\frac{54.164}{12.01} = 4.510$	$\frac{1.434}{1.008} = 1.423$	$\frac{2.895}{14.01} = 0.207$	$\frac{1.975}{32.06} = 0.062$	$\frac{26.954}{16.00} = 1.684$
Smallest ratio	$\frac{4.510}{0.062} = 72.742$	$\frac{1.423}{0.062} = 22.952$	$\frac{0.207}{0.062} = 3.339$	$\frac{0.062}{0.062} = 1$	$\frac{1.684}{0.062} = 27.161$
Simplest ratio	73	23	3	1	27
Sample	MOFs-W(OCH_2CH_3)$_6$/Ppy-rGO				
Percentage (%)	59.653	1.779	6.202	1.797	13.267
Number of moles (mol)	$\frac{59.653}{12.01} = 4.967$	$\frac{1.779}{1.008} = 1.765$	$\frac{6.202}{14.01} = 0.443$	$\frac{1.797}{32.06} = 0.056$	$\frac{13.267}{16.00} = 0.829$
Smallest ratio	$\frac{4.967}{0.056} = 88.696$	$\frac{1.765}{0.056} = 31.518$	$\frac{0.443}{0.056} = 7.911$	$\frac{0.056}{0.056} = 1$	$\frac{0.829}{0.056} = 14.804$
Simplest ratio	89	32	8	1	15

Notes: Molar mass for C: 12.01 g/mol; H: 1.008 g/mol; N: 14.01 g/mol; S: 32.06 g/mol and O: 16.00 g/mol

Table S4. Concentrations of the targeted analytes and the recorded charge transfer resistance.

N	Ammonium concentration (μM)	R_{CT} value (Ω)
1	0	258.49
2	0.85	422.27
3	1.26	467.63
4	1.68	670.71
5	2.52	734.45
6	3.35	854.64

Table S5. Weekly R_{CT} value for four weeks of the testing period.

Testing period	R_{CT} value of MOFs-W(OCH_2CH_3)$_6$/Ppy-rGO drop-casted SPE for trial (Ω)			Standard error	R_{CT} value of Ppy-rGO drop−casted SPE for trial (Ω)			Standard error
	1	2	3		1	2	3	
1st day	258.49	252.09	216.09	±22.857	198.27	198.78	310.61	±64.713
1st week	232.15	252.97	229.9	±12.720	205.14	201.22	314.66	±64.393
2nd week	234.7	256.53	233.69	±12.905	413.68	424.67	230.22	±109.232
3rd week	283.48	279.56	265.48	±9.466	434.26	433.47	236.23	±114.105
4th week	286.83	283.3	268.48	±9.737	246.38	291.39	170.1	±61.313

Before the determination of NH_4^+ ions, the effects of different experimental parameters, such as stability tests, reproducibility tests, and different scan rates, were studied and optimized. EIS is used for electrochemical performance studies. Meanwhile, CV is used to study the stability of a 2×10^{-3} wt% MOFs-W(OCH_2CH_3)$_6$/Ppy-rGO electrode with six concentrations of analytes: 0 μM, 1.26 μM, 0.84 μM, 1.68 μM, 2.52 μM and 3.35 μM. As predicted, higher concentration caused higher resistivity and, thus, low conductivity, as reported in the paper. The redox peak current has increased correspondingly to an increment of scan rate from 20 mVs^{-1} to 100 mVs^{-1}, as confirmed by linear regression with an R^2 of 0.9559 as shown in Figure S6A.

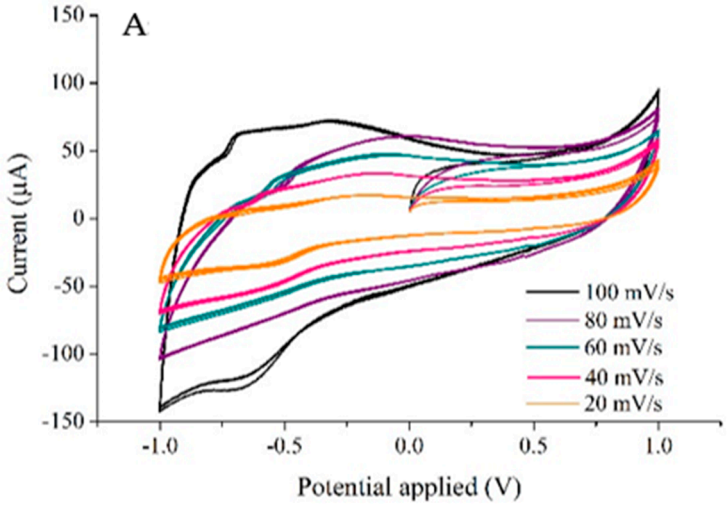

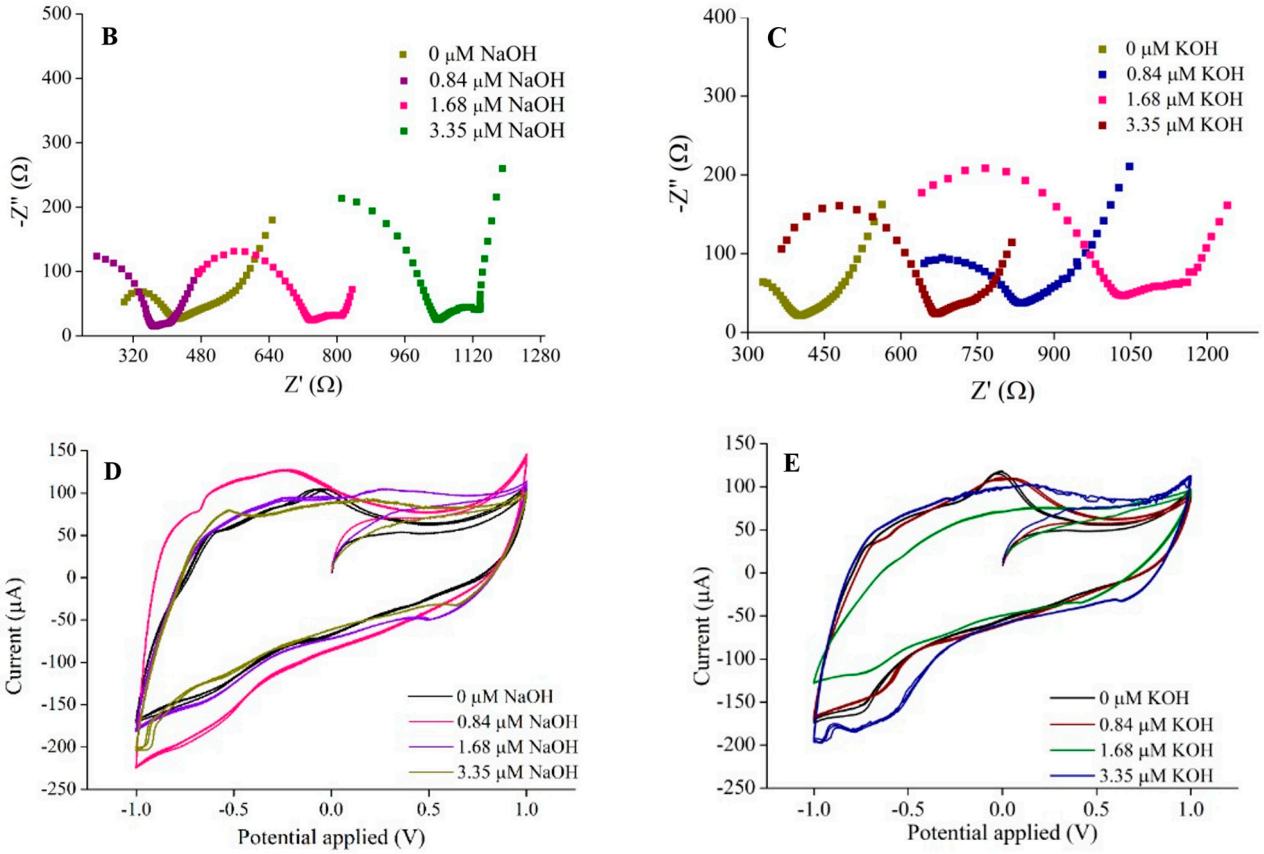

Figure S6. (**A**) CV curve of W-MOF/Ppy-rGO at different scan rates, EIS curve of MOFs-$W(OCH_2CH_3)_6$/Ppy-rGO drop-casted by (**B**) NaOH and (**C**) KOH analytes, and CV curve of (**D**) NaOH and (**E**) KOH analytes.

CV analyses of Na^+ and K^+ ion solutions were conducted at 100 mVs^{-1} to see the performance stability of the sensor upon detection of analytes at different concentrations. CV curves exhibit a quasi-rectangular shape without the presence of faradic peaks, which suggests the presence of double-layer capacitance. Double-layer capacitance (C_{dl}), which can also be expressed as a constant phase element (CPE), comes from the impedance if and only if the ideally polarizable electrode is represented as a connection of the R_s and C_{dl}. As a result, coupling of the resistance with the surface capacitance and adsorption of ions, as well as chemical inhomogeneities of the surface, occur. At similar scan rates (Figure S6C and S6D), the CV curve of each analyte showed slight distortion at certain concentrations, which displays slight consistency in electronic and ionic transport inside the supercapacitor electrode material caused by the analyte [6]. Both NaOH and KOH are strong bases that would completely dissociate in water or an aqueous solution. Hence, the analyte solution is very conductive and a bit corrosive to the surface of the MOFs-$W(OCH_2CH_3)_6$/Ppy-rGO nanocomposite. The CV and EIS curves are correlated to one another, which can be clearly seen because the lowest CV curves showed the highest R_s value.

Table S6. Reproducibility test with concentrations of the targeted analytes and the recorded charge transfer resistance.

Concentrations of the analyte (μM)	R_{CT} value for trial (Ω)			Standard error
	1	2	3	
0	331.27	162.29	258.49	±84.7601
0.84	398.01	220.18	422.27	±110.342
1.26	472.79	388.3	467.63	±47.361
1.68	753.02	532.52	670.71	±111.424

2.52	682.37	672.53	734.45	±33.274
3.35	1096.30	861.87	854.64	±137.483

Table S7. Selectivity test with concentrations of NH_4^+, Na^+, and K^+ analytes solution and recorded charge transfer resistance.

N	Concentration (μM)	R_{ct} value (Ω)		
		NH_4^+	Na^+	K^+
1	0	258.49	157.07	289.09
2	0.84	422.27	327.26	348.28
3	1.68	670.71	352.31	598.43
4	3.35	854.64	666.32	365.87

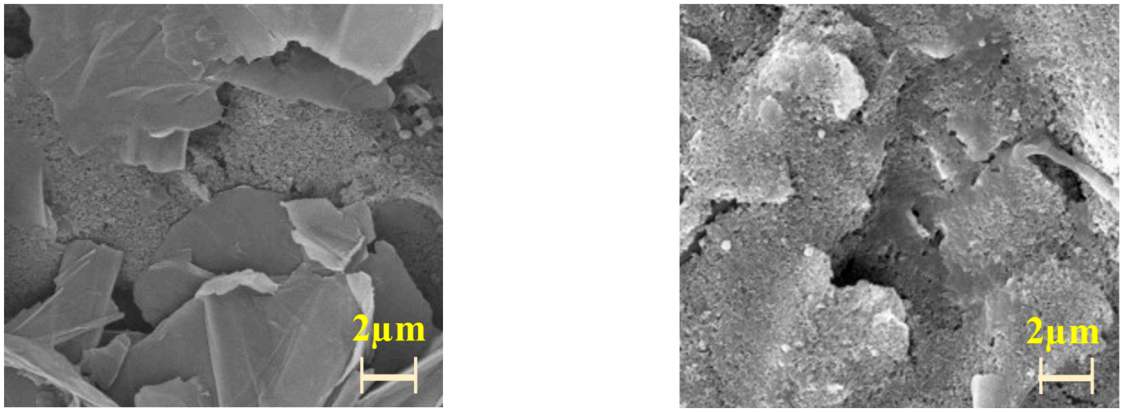

(**A**) (**B**)

Figure S7. FESEM images of (**A**) Ppy-rGO and (**B**) MOFs-W(OCH_2CH_3)$_6$/Ppy-rGO after degradation.

Table S8. The performance comparison of the W-MOF/Ppy-rGO-SPE device as an ammonium ions sensor with the developed ammonium ions sensor.

Materials	Technique	Concentration range	LOD	Type of sample	Ref.
Silver nanoparticles (AgNPs)	UV-Visible spectrophotometer and RGB analysis (colorimetrically)	10–1000 mgL^{-1}	180 mgL^{-1}–200 mgL^{-1}	Wastewater	[7]
PANI/Nafion/Cu_2O/SPE	Electrochemical Impedance Spectroscopy (EIS)	1–1000 μM	0.5 μM	Human serum	[8]
ZnO nanorod	Field-effect transistor (FET)	0.01 μM–2.5 mM	0.07 μM	Ammonium hydroxide in PBS buffer	[9]
Lipophilic cyclodextrin	CV, DPV, and SWV	4.2–66 μM	0.12 μM	Water/1,6-dichlorohexane micro-interface	[10]
Hybrid PVC-bentonite (mineral montmorillonite clay) thin film	FTIR spectroscopy, EDX, CV, and EIS	10^{-4} M–1 M	10^{-6} M	River	[11]
Photocured poly(n-butyl acrylate) membrane with immobilized nonactin	Spectrophotometry	10^{-1}–10^{-5} M	~10^{-6} M	Sewage	[12]

Gold nanoparticles (AuNPs) based on alanine dehydrogenase (AlaDH)	Amperometry and CV	0.1–0.5 mM	0.01 mM	Ammonium chloride	[13]
p-nitrobenzene-diazonium chloride	Spectrophotometry (Riegler's reagent)	10–60 ppm	7.9 ppm	River water	[14]
$CoCl_2.6H_2O$	Spectrophotometry	60–290 mM	16 mM	Polluted sewage water	[15]
Co^{2+} ions	Spectrophotometry	0.6–5.9 mM	-	NH_3 standard stock solution in deionized water	[16]
Glutamate dehydrogenase (GALDH) immobilized in chitosan film	Spectrophotometry (indothymol method)	0.005–0.5 mM	0.005 mM	Agricultural sample	[17]
W-MOF/Ppy-rGO	EIS and CV analyses	0–3.35 μM	0.278 μM	Spiked distilled water	This work

Abbreviations: RGB: red, green, and blue; Cu_2O: copper (I) oxide; ZnO: zinc oxide; $CoCl_2.6H_2O$: cobalt (II) chloride hexahydrate; Co^{2+}: cobalt ions.

References

1. Saheed, M.S.M.; Mohamed, N.M.; Singh, B.S.M.; Saheed, M.S.M. Precursor and pressure dependent 3D graphene: A study on layer formation and type of carbon material. *Diamond Relat. Mater.* **2017**, *79*, 93–101.
2. Wojtoniszak, M.; Chen, X.; Kalenczuk, R.J.; Wajda, A.; Łapczuk, J.; Kurzewski, M.; Drozdzik, M.; Chu, P.K.; Borowiak-Palen, E. Synthesis, dispersion, and cytocompatibility of graphene oxide and reduced graphene oxide. *Colloids Surf., B* **2012**, *89*, 79–85.
3. Zhu, Y.; Murali, S.; Cai, W.; Li, X.; Suk, J.W.; Potts, J.R.; Ruoff, R.S. Graphene and graphene oxide: synthesis, properties, and applications. *Adv. Mater.* **2010**, *22*, 3906–3924.
4. Zhang, Y.; Park, S.-J. In situ shear-induced mercapto group-activated graphite nanoplatelets for fabricating mechanically strong and thermally conductive elastomer composites for thermal management applications. *Composites Part A: Applied Science and Manufacturing* **2018**, *112*, 40–48.
5. Ansari, S.M.; Khan, M.Z.; Anwar, H.; Ikram, M.; Sarfraz, Z.; Alam, N.; Khan, Y. Tungsten Oxide–reduced Graphene Oxide Composites for Photoelectrochemical Water Splitting. *Arabian Journal for Science and Engineering* **2021**, *46*, 813–825.
6. Biswas, S.; Drzal, L.T. Multilayered nanoarchitecture of graphene nanosheets and polypyrrole nanowires for high performance supercapacitor electrodes. *Chem. Mater.* **2010**, *22*, 5667–5671.
7. Amirjani, A.; Fatmehsari, D.H. Colorimetric detection of ammonia using smartphones based on localized surface plasmon resonance of silver nanoparticles. *Talanta* **2018**, *176*, 242–246.
8. Zhybak, M.T.; Vagin, M.Y.; Beni, V.; Liu, X.; Dempsey, E.; Turner, A.P.; Korpan, Y.I. Direct detection of ammonium ion by means of oxygen electrocatalysis at a copper-polyaniline composite on a screen-printed electrode. *Microchim. Acta* **2016**, *183*, 1981–1987.
9. Ahmad, R.; Tripathy, N.; Khan, M.Y.; Bhat, K.S.; Ahn, M.-s.; Hahn, Y.-B. Ammonium ion detection in solution using vertically grown ZnO nanorod based field-effect transistor. *RSC Adv.* **2016**, *6*, 54836–54840.
10. Ribeiro, A.; Silva, F.; Pereira, C.M. Electrochemical sensing of ammonium ion at the water/1, 6-dichlorohexane interface. *Talanta* **2012**, *88*, 54–60.
11. Zazoua, A.; Kazane, I.; Khedimallah, N.; Dernane, C.; Errachid, A.; Jaffrezic-Renault, N. Evidence of ammonium ion-exchange properties of natural bentonite and application to ammonium detection. *Mater. Sci. Eng., C* **2013**, *33*, 5084–5089.
12. Heng, L.Y.; Alva, S.; Ahmad, M. Ammonium ion sensor based on photocured and self-plasticising acrylic films for the analysis of sewage. *Sens. Actuators, B* **2004**, *98*, 160–165.
13. Ling, T.L.; Ahmad, M.; Heng, L.Y.; Seng, T.C. The effect of multilayer gold nanoparticles on the electrochemical response of ammonium ion biosensor based on alanine dehydrogenase enzyme. *Journal of Sensors* **2011**, *2011*, 754171.
14. Tan, L.L.; Musa, A.; Lee, Y.H. Reflectance based optical fibre sensor for ammonium ion using solid-state Riegler's reagent. *Sens. Actuators, B* **2012**, *173*, 614–619.
15. Tan, L.L.; Ahmad, M.; Lee, Y.H. A novel optical ammonia sensor based on reflectance measurements for highly polluted and coloured water. *Sens. Actuators, B* **2012**, *171*, 994–1000.
16. Ling, T.L.; Ahmad, M.; Heng, L.Y. UV-vis spectrophotometric and artificial neural network for estimation of ammonia in aqueous environment using cobalt (II) ions. *Anal. Methods* **2013**, *5*, 6709–6714.
17. Azmi, N.E.; Ahmad, M.; Abdullah, J.; Sidek, H.; Heng, L.Y.; Karuppiah, N. Biosensor based on glutamate dehydrogenase immobilized in chitosan for the determination of ammonium in water samples. *Anal. Biochem.* **2009**, *388*, 28–32.